Quantitative Decoupling of Oxygen-Redox and Manganese-Redox Voltage Hysteresis in a Cation-Disordered Rock Salt Cathode

*Tzu-Yang Huang, Zijian Cai, Matthew J. Crafton, Lori A. Kaufman, Zachary M. Konz, Helen K. Bergstrom, Elyse A. Kedzie, Han-Ming Hao, Gerbrand Ceder, Bryan D. McCloskey**

T.-Y. Huang, M. J. Crafton, L. A. Kaufman, Z. M. Konz, H. K. Bergstrom, E. A. Kedzie, B. D. McCloskey
Department of Chemical and Biomolecular Engineering
University of California-Berkeley
Berkeley, CA 94720, USA
Email Address: bmcclosk@berkeley.edu

T.-Y. Huang, M. J. Crafton, L. A. Kaufman, Z. M. Konz, H. K. Bergstrom, E. A. Kedzie, B. D. McCloskey
Energy and Distributed Resources Division
Lawrence Berkeley National Laboratory
Berkeley, CA 94720, USA

Z. Cai, H.-M. Hao, G. Ceder
Department of Materials Science and Engineering
University of California-Berkeley
Berkeley, CA 94720, USA

Z. Cai, H.-M. Hao, G. Ceder
Materials Sciences Division
Lawrence Berkeley National Laboratory
Berkeley, CA 94720, USA

Keywords: *lithium-ion battery, energy efficiency, anionic redox, titration, mass spectrometry*

Abstract

Pronounced voltage hysteresis in Li-excess cathode materials is commonly thought to be associated with oxygen redox. However, these materials often possess overlapping oxygen and transition-metal redox, whose contributions to hysteresis between charge and discharge are challenging to distinguish. In this work, a two-step aqueous redox titration was developed with the aid of mass spectrometry (MS) to quantify oxidized lattice oxygen and $Mn^{3+/4+}$ redox in a representative Li-excess cation-disordered rock salt — $Li_{1.2}Mn_{0.4}Ti_{0.4}O_2$ (LMTO). Two MS-countable gas molecules evolve from two separate titrant-analyte reactions, thereby allowing Mn and O redox capacities to be decoupled. The decoupled O and Mn redox coulombic efficiencies are close to 100% for the LMTO cathode, indicating high charge-compensation reversibility. As incremental Mn and O redox capacities are quantitatively decoupled, each redox voltage hysteresis is further evaluated. Overall, LMTO voltage hysteresis arises not only from an intrinsic charge-discharge voltage mismatch related to O redox, but also from asymmetric Mn-redox overvoltages. The results reveal that O and Mn redox both contribute substantially to voltage hysteresis. This work further shows the potential of designing new analytical workflows to experimentally quantify key properties, even in a disordered material having complex local coordination environments.

This is the author manuscript accepted for publication and has undergone full peer review but has not been through the copyediting, typesetting, pagination and proofreading process, which may lead to differences between this version and the Version of Record. Please cite this article as doi: 10.1002/aenm.202300241

1 Introduction

In the global movement toward electrifying transportation, three of the major determinants for viable electric-vehicle (EV) batteries are cell cost, energy density, and energy efficiency. These factors are governed mostly by the cathode material for typical Li-ion batteries.[1] As EV cell cathodes are overwhelmingly stoichiometric-layered chemistries ($LiMO_2$, M = Ni, Co, Mn, Al), limited cobalt and nickel resources[2,3] have raised concerns over impending supply disruptions that can result in cell cost volatility.[4] As a result, adopting low-cost and sustainable raw materials for cathodes in Li-ion batteries has become particularly important for ongoing research and development. One prominent type of emerging cathode material is Li-excess cation-disordered rock salts (DRX),[5–7] because they can accommodate diverse earth-abundant transition-metal (TM) compositions that include predominantly inexpensive metals, such as Mn and Ti,[8,9] while at the same time exhibiting high gravimetric energy densities that approach 1000 Wh kg^{-1}.[10] Despite their high achievable energy densities with low-cost compositions, DRX materials' inherent cation site mixing not only induces non-uniform Li site energies,[11] but also activates concurrent TM-redox and oxygen-redox charge compensation mechanisms.[12–14] Together, these diverse characteristics among DRX materials lead to a wide variety of capacity and voltage characteristics, particularly voltage gaps between galvanostatic (constant current) charge and discharge curves.[6,15] This phenomenon, commonly termed voltage hysteresis, diminishes the operating energy efficiency of DRX cathodes.

Voltage hysteresis can be clearly visualized by plotting charging and discharging voltage V against cumulative capacity q, which is defined here as the net amount of electrons transferred from the cathode to the external circuit, for incremental electric charge $dq > 0$ on charging (Chg) and $dq < 0$ on discharging ($Dchg$):

$$q = \int_{Chg} dq + \int_{Dchg} dq \tag{1}$$

At a definite voltage V, incremental capacity dq is measurable by an externally connected potentiostat, but internally dq is ultimately redistributed and compensated by a set of redox-active species, denoted with i, such as TM and O in the DRX material:

$$dq = \sum_i dq_i \tag{2}$$

Among various redox-mechanism studies for alkali transition-metal oxide cathodes, recent spectroscopic and ab initio research has provided evidence correlating voltage hysteresis with oxygen redox, in which the lattice oxygen is oxidized to form various species (e.g., trapped O_2[13,16] or non-dimerized O^-[17,18]) accompanied with varying local coordination (e.g., TM migration,[12,19,20] defect formation,[21] or ligand-to-metal charge transfer[22]). However, few studies can experimentally decouple and quantify the incremental capacity contributions from both TM and O redox (dq_i in Equation (2)), particularly if these redox processes simultaneously occur at a given voltage. Mixed redox contributions can also complicate X-ray spectroscopy analysis, where overlapping photon-signal features are difficult to translate into each redox capacity. Therefore, dq_i remains a critical piece of missing information for studying voltage hysteresis as well as improving round-trip energy efficiency. As the charge-discharge voltage mismatch changes with capacity q, varying redox combinations $\sum_i dq_i$ along the q axis implies that each redox mechanism i can have different round-trip energy efficiency η_i, as defined below:

$$\eta_i = \frac{-\int_{Dchg} V dq_i}{\int_{Chg} V dq_i} \tag{3}$$

In other words, acquiring deconvoluted energy efficiency η_i will allow us to evaluate how each redox mechanism i impacts voltage hysteresis once we decouple TM and O redox capacity contributions, dq_i.

To address this challenge, we re-designed a conventional aqueous redox titration with the aid of a mass spectrometry (MS) gas analyzer to quantify the amount of solid-phase oxidized oxygen and $Mn^{3+/4+}$ individually within a representative Mn-based DRX material, $Li_{1.2}Mn_{0.4}Ti_{0.4}O_2$. This novel two-step titration on cathodes evolves two distinguishable gas molecules, which are quantifiable by the MS gas analyzer. For the DRX cathodes at varying states-of-charge, each of the two titration reaction stoichiometries allows backcalculation of the Mn-redox and O-redox capacities, separately. We then measured the cathode's voltage during galvanostatic cycling, as well as at quasi-equilibrium of various states of charge. Deconvoluted voltage hysteresis of each redox process is presented by plotting voltages against decoupled capacities, q_i. At the end of this work, redox hysteresis curves enable us to decouple redox energy efficiencies, η_i, as well as redox overvoltage distributions, which unambiguously informs how each redox mechanism contributes to the overall voltage hysteresis. Our results show promise of designing new analytical workflows to experimentally evaluate overlapping capacity contributions, even in a DRX material having complex local coordination environments. Thus, we anticipate that our titration design strategies can be further extended to other cathode chemistries involving mixed TM and oxygen redox.

2 Results and Discussion

2.1 Titration Design by Analyte's Aqueous Instability

Conventional aqueous redox titrations, such as the iodometric titration,[23,24] were designed on the basis of fast (in a few seconds) electron-transfer reactions between the titrant and analyte solution in a single-phase liquid environment. To quantify oxidant analytes in the solid phase — i.e., oxidized oxygen and $Mn^{3+/4+}$ in the DRX material — adopting a regular redox titration is challenging due to the oxide materials' low aqueous solubility, where slow heterogeneous reaction kinetics between the solid analyte and liquid titrant becomes susceptible to interference by other non-negligible side reactions (e.g., ambient air slowly oxidizes iodide in iodometry[25]). In light of the limitation described above, we re-examined the solution chemistry by blending appropriate titrants to effectively destabilize each solid-phase analyte under specific aqueous conditions, accompanied with characteristic gas release as detailed in the following sections.

2.1.1 Frost Diagram

Solid-phase oxidized oxygen species existing in TM oxides have been shown to be unstable and evolve substantial O_2 gas in strong aqueous acid[26,27] when concentrated proton H_3O^+ replaces mobile lattice Li^+.[28] This self-decomposition is well predicted by the aqueous thermodynamic stability of elemental oxygen with various formal oxidation numbers N, as is visualized by a Frost diagram[29] plotting free energies (N multiplied by electrochemical potential relative to O_2) of different oxidation states shown in **Figure 1a**. If three participating states form a concave-down connection in **Figure 1a** (e.g., $H_2O \leftarrow H_2O_2 \rightarrow O_2$), disproportionation of a certain state into two neighboring states, where net change of N in both positive and negative directions equals zero, is thermodynamically favorable. Ultimately, regardless of oxidation numbers, aqueous oxidized oxygen species are prone to disproportionate all the way to end members H_2O and O_2.

The thermodynamic instability predicted by the Frost diagram is applicable to oxidized oxygen existing in a solid DRX material because we have previously used isotopic labelling to study ^{18}O-enriched DRX materials and have unambiguously shown that DRX-derived O_2 gas release during strong acid titration can accurately estimate oxygen-redox capacity.[30] The back-calculation is based on the following two equations, where other elements (Li and TM) in the DRX solid are not shown in the formula for clarity and the electrochemical cell hosts the electron-transfer reaction:

$$2\,O^{2-}(s) \underset{Dchg}{\overset{Chg}{\rightleftharpoons}} 2\,O^{n-}(s) + 2(2-n)\,e^- \tag{4}$$

Here, $0 \leq n < 2$. Two O^{n-} (s) can be either dimerized or non-dimerized. We posit that with strong aqueous acid surrounding it during the titration, relaxed O^{n-} in the aqueous environment preferentially dimerize due to a closer frontier-orbital energy and symmetry match,[31] which is followed by disproportionation-derived O_2 release from the ex-situ cathode:

$$2\,O^{n-}(s) + 2n\,H_3O^+(aq) \xrightarrow{\text{aqueous acid}} 3n\,H_2O(l) + \frac{2-n}{2}\,O_2(g) \quad (5)$$

Therefore, cumulative O-redox capacity $2(2-n)$ is linearly correlated with the quantity of O_2 released during a strong acid titration. Moreover, the linear relationship between O-redox and O_2 is independent

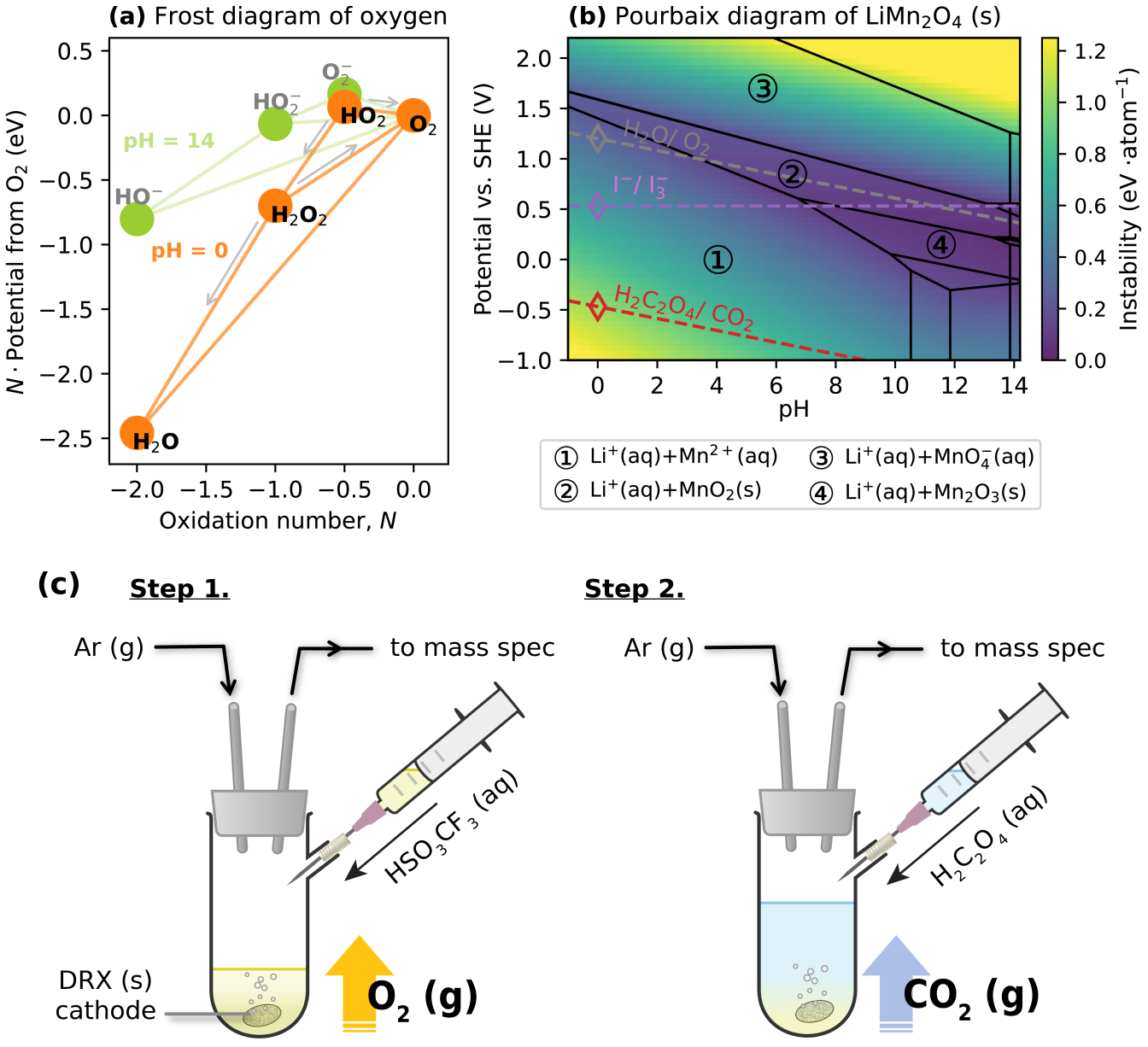

Figure 1: Two-step titration design to quantify O and Mn redox. (a) Oxygen Frost diagram in basic and acidic aqueous solutions. Formal oxidation number N of oxygen varies horizontally, while the vertical axis presents N multiplied by the standard half-reaction potential between each state and O_2. (b) Li-Mn-O-H Pourbaix diagram overlaid with a spinel $LiMn_2O_4$ instability map, where the suffix (s) or (aq) denotes the material phase. The diagram is generated computationally, as described in the Experimental Section. (c) Illustration of two-step titration mass spectrometry (TiMS) and its experimental setup. Strong aqueous acid HSO_3CF_3 (triflic acid) destabilizes solid-phase oxidized oxygen upon the first injection. The second injection involves reaction between solid-phase $Mn^{3+/4+}$ and oxalic acid, which produces CO_2. Characteristic O_2 or CO_2 released from each analyte-titrant reaction is quantifiable by the mass-spectrometry gas analyzer.

of formal oxidation state $n-$, (O-capacity divided by O_2 quantity is invariant, $2(2-n)\cdot(\frac{2-n}{2})^{-1}=4$) which allows quantification of solid-phase oxidized oxygen from Equation (4) with any n in $0 \leq n < 2$. The wide-range applicability further suggests that our titration design is generizable for quantifying O-redox capacity originating from various oxidized oxygen species in the solid phase.

2.1.2 Pourbaix Diagram

Solid-aqueous equilibria is used to predict solid materials' stability (corrosion or passivation) in various aqueous environments, where the most thermodynamically stable phases at a given pH value and applied potential can be displayed on a Pourbaix diagram.[32] To access $Mn^{3+/4+}$ within the bulk of solid DRX materials in our titration design, the titrant solution must be optimized to effectively disintegrate the solid DRX analyte in solution. Here we first analyzed a Pourbaix diagram for cation-ordered spinel $LiMn_2O_4$ in **Figure 1b** (see Experimental Section for computational details[33–35] of generating the plot). We anticipated that $LiMn_2O_4$-aqueous equilibria will be similar to $Li_{1.2}Mn_{0.4}Ti_{0.4}O_2$-aqueous equilibria, as the redox-active Mn in each material possesses similar oxidation states, with octahedral coordination to a rock-salt-like anion lattice.

When spinel $LiMn_2O_4$ is immersed in the acid titrant with trace O_2, an aqueous environment surrounds the solid with pH ≈ 0 and $\sim$1.20 V vs. SHE, due to the H_2O/O_2 equilibrium potential that is naturally established near the $LiMn_2O_4$ surface. This condition is labelled by the grey diamond marker in **Figure 1b**. Here, the solid-phase $LiMn_2O_4$ (with Mn in a mixture of +3 and +4 states) is prone to transform into aqueous Li^+ and Mn^{2+}. However, instead of forming fully transparent solution, experimentally the spinel manganese oxide remains in the undissolved and dispersed solid phase, as shown by **Figure S1a** in the Supporting Information (SI). This result agrees with the material's low thermodynamic instability in acid, which can be visually captured by a computed relative free energy map,[34] as displayed at the grey diamond marker in **Figure 1b**: 0.30 eV atom^{-1} (with a positive free energy denoting the material's instability). In addition, during an acid titration with H_2SO_4 as the titrant, we did not observe O_2 gas from water splitting ($2H_2O$ (l) $\rightarrow$ O_2 (g) + $4H^+$ + $4e^-$, SI **Figure S2a**), which should be the most probable aqueous charge-compensating redox couple[30] for $Mn^{3+/4+}$ reduction without an external circuit. No water-derived O_2 release indicates no decomposition reaction involving electron transfer to solid-phase $Mn^{3+/4+}$ (e.g., Mn^{3+} (s) + e^- $\rightarrow$ Mn^{2+} (aq)). Therefore, to decompose and reduce solid-phase $Mn^{3+/4+}$, the acid titrant must be adjusted to promote solid-phase thermodynamic instability.

Along the vertical axis of the relative free energy map, lowering the aqueous equilibrium potential near the solid oxide surface is clearly the most effective way to push the spinel solid phase towards higher instability, as shown in **Figure 1b** by moving the diamond marker downwards to the brighter region. To this end, we introduced an aqueous reductant, oxalic acid, to effectively lower the aqueous equilibrium potential. Here oxalic acid was specifically selected instead of a regular redox titrant such as potassium iodide, because our titration design requires several of the properties possessed by aqueous $H_2C_2O_4$. First, the low equilibrium potential of aqueous $H_2C_2O_4$ adequately enhances the thermodynamic instability of $LiMn_2O_4$. While a conventional redox titrant with I^-/I_3^- results in a $LiMn_2O_4$ instability energy 0.59 eV atom^{-1} larger than the 0.30 eV atom^{-1} found under pure acidic conditions, (**Figure 1b**) the spinel instability at the $H_2C_2O_4/CO_2$ equilibrium line increases to 1.02 eV atom^{-1}, providing a large driving force for material disintegration in solution. Second, the $H_2C_2O_4$ redox titration product is CO_2 gas, which can be easily separated from the analyte-titrant mixture under acidic conditions and thus is reliably quantifiable. Removing CO_2 gas from the solution also ensures that the titration proceeds to a greater extent of reaction, following Le Chatelier's principle. Third, carbon atoms in the redox couple $H_2C_2O_4/CO_2$ carry explicit formal charges, which warrants unambiguous charge-compensation stoichiometry. Unlike other organic acid candidates such as citric acid, the change of carbon oxidation states from $H_2C_2O_4$ (3+) to CO_2 (4+) is readily traceable. Overall, oxalic acid's unique characteristics listed above make it exceptionally suitable for quantifying solid-phase $Mn^{3+/4+}$.

The stoichiometry to quantify Mn redox using oxalic acid as a titrant is outlined via the following

two equations, where electron transfer to/from Mn first occurs in an electrochemical cell, with α being a constant (fixed for each material) and defined as the number of Mn^{3+} per unit formula in the as-prepared cathode material:

$$Mn_{\alpha}^{3+}(s) \underset{Dchg}{\overset{Chg}{\rightleftharpoons}} Mn_{\alpha}^{(3+\frac{m}{\alpha})+}(s) + m\,e^{-} \quad (6)$$

For clarity of Equation (6), we do not show other elements (e.g., Li and O) in the expression. Here solid-phase $Mn^{3+/4+}$ reacts with $H_2C_2O_4$ to release CO_2 gas when the cathode is titrated as depicted in **Figure 1c**:

$$Mn_{\alpha}^{(3+\frac{m}{\alpha})+}(s) + \frac{m+\alpha}{2} H_2C_2O_4(aq) \longrightarrow (m+\alpha)\,H^{+}(aq) + \alpha\,Mn^{2+}(aq) + (m+\alpha)\,CO_2(g) \quad (7)$$

Cumulative Mn-redox capacity varies linearly with the amount of oxalate-derived CO_2 evolved, ($q_{Mn} = m$; $q_{Mn} = CO_2 - \alpha$), which we verify through titration experiments on spinel $LiMn_2O_4$ cathodes at various states-of-charge (See SI **Figure S2**). Such experimental agreement shows the promise of quantifying Mn-capacity, particularly in the Mn-based DRX material, by our oxalic-acid titration design.

2.1.3 Two-Step Titration Mass Spectrometry (TiMS)

Based on our designed titrations, disproportionation-derived O_2 and oxalate-derived CO_2 measure solid-phase oxidized oxygen and $Mn^{3+/4+}$, respectively. To quantify two coexisting solid analytes, the aqueous environment surrounding the immersed DRX cathode must be controlled for each of the designed reactions to avoid crossover interference. Namely, preventable errors may take place if unintended reactions, such as that between O^{n-} and $H_2C_2O_4$, were not taken into consideration. We therefore titrated each extracted cathode with sequential injections of strong acid followed by oxalic acid, where the two steps are separated by multiple hours to better control each analyte-titrant reaction. The first injection uses a strong aqueous acid, which destabilizes solid-phase oxidized oxygen species and releases associated O_2 gas (referred to here as disp-O_2). Besides allowing oxidized oxygen quantification, the strong aqueous acid decomposes surface carbonate species, which inevitably remain as synthesis impurities and electrolyte-degradation products.[36] Surface carbonate species reacts with the strong acid titrant to evolve CO_2 gas, which we term carbonate-CO_2. Both carbonate-CO_2 and disp-O_2 were continuously monitored and removed (**Figure 1c**) from the titration vessel headspace until their MS signals completely attenuated, eliminating the presence of carbonate and oxidized oxygen for the following step. Next, as shown in **Figure 1c**, oxalic acid was injected to reductively decompose the remaining $Mn^{3+/4+}$ in the solid oxide, which releases CO_2 (oxalate-CO_2) downstream in this second step. As a result of our two-step titration setup, we limit crossover interference between the two major analyte-titrant reactions, which enables decoupling of the two redox capacities as calculated from disp-O_2 and oxalate-CO_2.

To distinguish and quantify each characteristic gas molecule, we attached our titration vessel to a gas-handling system equipped with a highly sensitive (detection limit $\geq$ 0.02 mol%) quadrupole mass spectrometer.[30] Moreover, if any unexpected gas (other than O_2 and CO_2) evolved during titration, our MS gas analyzer could readily detect and identify any possible side reactions. Indicators of side reactions were crucial during the early stage of our titration design, because these side reactions are likely to introduce interference. For example, when nitric acid was initially used as the strong acid titrant in the first step, over 100% yield of oxalate-CO_2 accompanied nitrogen monoxide gas release upon oxalic acid introduction in the second step. In this case, the nitrate anion was obviously the source of the unintended NO gas, which directed us to other strong acids having anions compatible with aqueous oxalic acid. For this reason, triflic acid (HSO_3CF_3 (aq)) was selected as the strong acid titrant due to its extremely negative pKa.[37] See the SI Note S1, Note S2, and **Figure S3-S5** for details of optimizing $Mn^{3+/4+}$-oxalate reaction conditions with the aid of our MS gas analyzer. Once the titration conditions were optimized, mass spectrometry was combined with the two-step titration design (which we term titration mass spectrometry, or TiMS) to enable the quantification of solid-phase O and Mn redox.

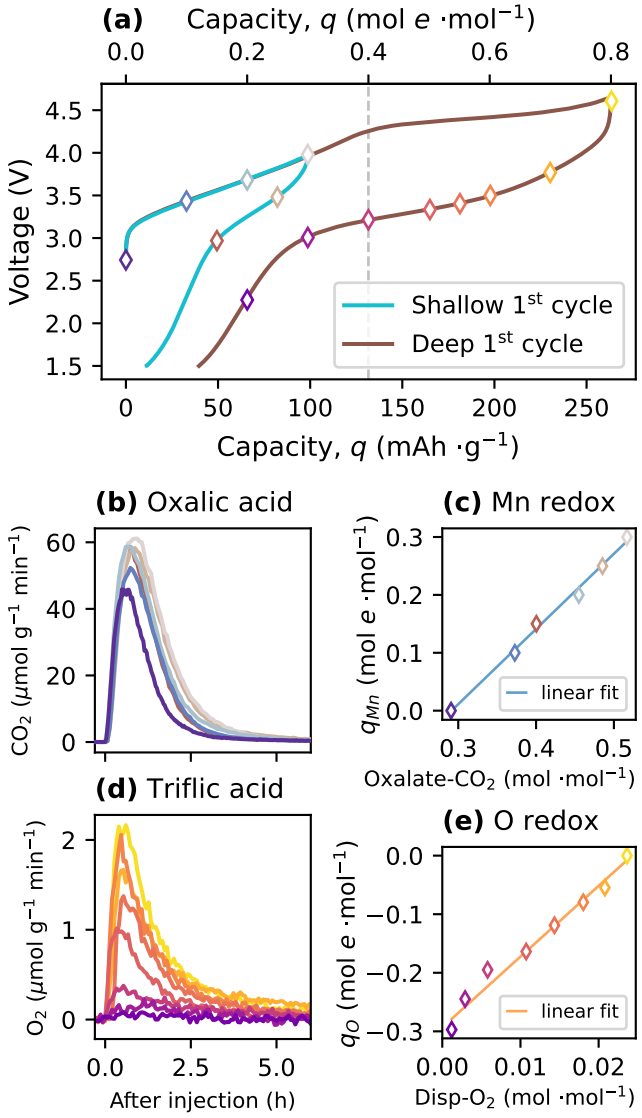

Figure 2: Capacity decoupling for the cation-disordered rock salt $Li_{1.2}Mn_{0.4}Ti_{0.4}O_2$ (LMTO) via titration mass spectrometry (TiMS). (a) First-cycle voltage profiles of LMTO. The vertical dashed line marks the expected maximum Mn capacity if it were the exclusive charge compensation mechanism. Diamond markers denote cathode extraction points from various cells at different state of charge. (b) Oxalate-CO_2 evolution curves from applying 2-step TiMS on cathodes cycled within the first shallow cycle. (c) Linear regression between shallow-cycle Mn capacity and oxalate-CO_2: $q_{Mn} = 1.2993 \cdot CO_2 - 0.3786$; $R^2 = 0.9944$. Data points are color-coded to match pure Mn capacities in Figure 2a and TiMS CO_2 curves in Figure 2b, c. (d) Disp-O_2 evolution curves from applying 2-step TiMS on cathodes discharged within the first deep cycle. (e) Linear regression between discharge O capacity and disp-O_2: $Dchg\ q_O = 12.079 \cdot O_2 - 0.2932$; $R^2 = 0.9799$. Discharge O capacities were derived from Equation (8), where the interfacial parasitic reaction contribution is negligible. Data points are color-coded to match extraction states in Figure 2a and TiMS O_2 curves in Figure 2d, e.

2.2 Decoupling Mixed Redox Capacities

Coexisting Mn and O redox have been shown as the major charge compensation mechanisms[15] in our DRX material $Li_{1.2}Mn_{0.4}Ti_{0.4}O_2$ (LMTO; SI **Figure S7**). For Mn-based DRX materials undergoing first charge, each redox capacity is challenging to quantify independently at higher states of charge (SOC), because high-voltage side reactions complicate any decoupling effort due to a sizable capacity contribution from parasitic processes at the cathode-electrolyte interface[27] (all side reactions other than Mn and O redox, $dq_{side} \neq 0$). Here we first limited parasitic reactions by cycling LMTO within a shallow SOC range, as displayed in **Figure 2a**. The capacity is plotted on the upper x-axis in a molar electric charge unit, mol e mol^{-1} (moles of electrons per mole of active material LMTO), because in this work we mostly adjust SOC by $dq = 0.1$ mol e mol^{-1} (32.9 mAh g^{-1}) to study LMTO cathodes at different

SOC. In **Figure 2**, LMTO cathodes are charged and discharged to the points indicated by each diamond marker in **Figure 2a**. The cathodes are then extracted from the cell, lightly rinsed, and subjected to the 2-step titration depicted in **Figure 1c**. In the shallow capacity range ($q \leq 0.3$) during charge, our differential electrochemical mass spectrometry (DEMS) shows very minor in-situ CO_2 evolved from interfacial degradation processes, ($<$ 2 mmol mol^{-1}, SI **Figure S8a**) which indicates negligible parasitic reaction capacity contributions in this SOC range. In addition to limited side reactions, there is minimal O-redox activity: neither in-situ gaseous O_2 loss (SI **Figure S8a** by DEMS) nor solid-phase oxidized oxygen (**Figure 3a** by TiMS) is observed in the low SOC range. Therefore, the shallow-SOC capacity essentially represents pure Mn-redox capacity (measurable by a potentiostat, $q = q_{Mn}$), which is linearly correlated with TiMS oxalate-CO_2, as displayed in **Figure 2b, c**.

The oxalate-CO_2 linear regression slope and its y-intercept as a function of Mn capacity allow us to obtain two interpretable properties: the LMTO-oxalate reaction yield, and the average Mn oxidation state in the as-prepared LMTO cathode, the calculations of which are both detailed in SI Note S3. We note here that the as-prepared LMTO is expected to have Mn in its +3 state, which can be derived such that the expected y-intercept should cross $q_{Mn} = -0.4$ (SI **Figure S6a**) given the stable reaction yield (slope = a constant). Our results show a close-to-expected y-intercept of -0.3786, which gives an average Mn valence in the as-prepared state of +2.95, indicating that the targeted composition was largely achieved during synthesis of LMTO. Most importantly, shallow-cycled LMTO and its oxalate-CO_2 linear regression enable us to predict Mn-redox capacity q_{Mn} over the entire SOC range with mixed redox contribution, because our two-step titration and back-calculation intrinsically limits crossover interference from the other major capacity contribution — O redox, whose exact linear correlation with disp-O_2 from cycled LMTO is also required to enable accurate quantification.

To extract the O capacity from mixed redox contributions, we characterized various discharge states after charging LMTO cathodes to an identical state (0.8 Li^+ removed per unit LMTO, **Figure 2a**). Because cathode-electrolyte interfacial degradation has been identified mostly during high-voltage charge,[38–40] we characterize O-redox on discharge to suppress any interference due to parasitic processes, allowing us to assume $dq_{side} = 0$ in Equation (2)). In other words, discharge O capacity can be derived from potentiostat-measurable net discharge capacity and oxalate-measurable Mn capacity:

$$\int_{Dchg} dq_O = \int_{Dchg} dq - \int_{Dchg} dq_{Mn} \tag{8}$$

Between the extracted O capacity using Equation (8) and disp-O_2 measured at each diamond marker in the deep first cycle, there is a clear linear correlation as shown in **Figure 2a, d, e**. Here disp-O_2 linear regression is applicable to other SOC ranges over the entire charge-discharge cycle, due to analogous reasoning for the oxalate-CO_2 titration. As a result, each characteristic gas from TiMS has its own linear correlation with the corresponding redox capacity in LMTO, which further enables capacity decoupling in any SOC range and cycle.

2.2.1 First-Cycle Redox Components

The first (formation) cycle of LMTO shows a unique voltage profile compared to subsequent cycles, (SI **Figure S9**) as both the DRX bulk[12] and surface[27,41] undergo permanent change. To clearly capture formation-cycle evolution in terms of redox contributions, we present first-charge and first-discharge data separately in **Figure 3** by plotting decoupled capacities q_i (i = Mn and O redox, in-situ O_2 gas loss, or parasitic processes) vs. net capacity q. Although q_i data are discrete in our method, dq_i (the difference between adjacent data points) is adequate for numerical integration and differentiation, which provides accurate approximation of redox capacity contributions with a reasonable lab-scale throughput. As displayed by orange markers in **Figure 3**, O-redox capacity was translated from TiMS disp-O_2; Mn-redox capacity was calculated from oxalate-CO_2 (blue markers), which together allow visualization of decoupled redox capacity trends. In addition, we used DEMS to quantify the capacity of in-situ

gaseous O_2 loss, which is a minor contributor to overall O redox (solid-phase oxidized oxygen + in-situ gaseous O_2). The parasitic contribution is defined as all other capacities not accounted for, which also reflects propagation of errors from Mn and O capacity back-calculation, during the first-cycle charge and discharge.

Upon charge, Mn capacity initially grows along the parity line (net capacity) in **Figure 3c**, until q_{Mn} hits 0.3 mol e mol^{-1}. In the following SOC range (0.3-0.5 mol e mol^{-1}), Mn redox stagnates well before Mn capacity reaches its expected maximum (0.4 mol e mol^{-1}), which confirms that not all solid-phase Mn has been oxidized to the 4+ state (the average Mn oxidation state remains around 3.68+). Instead of further Mn-redox contributions after $q \geq 0.3$ mol e mol^{-1}, an increase in parasitic capacity contribution is observed, followed closely by O-redox contributions at $q \geq 0.4$ mol e mol^{-1}. The later onset of q_O than q_{side} possibly suggests that oxidized oxygen may only be stable after surface passivation that arises due to parasitic processes. Although surface parasitic capacity dominates in the static-q_{Mn} range (0.3-0.5 mol e mol^{-1}), q_{side} soon plateaus at around 0.11 mol e mol^{-1}, followed by O-redox capacity growth and a revival of Mn redox. Ultimately, q_{Mn} is close to its expected maximum, while q_O increases steadily to 0.29 mol e mol^{-1} at the end of the first charge. Overall, the Mn capacity trend agrees with ab initio calculations by Sharpe et al.,[13] who presented Mn oxidation under similar DRX local coordination (**Figure 3c** in this work vs. Figure 4c in the reference[13]). Furthermore, other studies have linked DRX material's O redox to Mn migration.[12,42] Although Mn migration is not favored by Mn^{4+} due to the large activation energy barrier to move out of an octahedral ligand field,[43] our Mn-capacity accounting indicates that at the O-redox onset there exist at least some Mn^{3+} or Mn^{2+}, which both have a smaller energy barrier to move, if any,[12,42] than Mn^{4+}. Moreover, a plausible link between TM migration and the parasitic processes could exist, although establishing this relationship requires more advanced spectroscopic tools outside the scope of the current study. These validations suggest that our titration design is suitable to quantify Mn-redox capacity in DRX cathodes experimentally. In addition to TiMS experiments, our DEMS measurements reveal negligible in-situ O_2 gas loss ($<$ 0.5 mmol mol^{-1}, SI **Figure S8b**), which confirms that solid-phase oxidized oxygen is the major contributor to O-redox capacity across the high SOC range.

Now turning to the first discharge, with an operating voltage window of 4.55-1.50 V (**Figure 2a**), we present decoupled capacities as a function of net discharge capacity ($Dchg\ q = \int_{Dchg} dq < 0$, **Figure 3f**) after an initial charge to 0.8 mol e mol^{-1}. As the minor discharge q_{side} in **Figure 3f** fluctuates mostly within the propagated error from all capacity back-calculations, net discharge capacity (parity dashed line) is closely followed by the sum of Mn and O capacities. Both redox mechanisms substantially contribute to charge compensation across nearly all of the discharge SOC range, in stark contrast to the charge compensation trends observed during the first charge. For example, the static-q_{Mn} range described earlier spans the middle 0.2 mol e mol^{-1} during first charge, while the analogous static range is narrower ($-0.3 \leq Dchg\ q \leq -0.2$ mol e mol^{-1}) during discharge. Although the Mn and O discharge redox curves do not mirror first charge, each has a round-trip coulombic efficiency (CE_i) close to 100%:

$$CE_i = \frac{-\int_{Dchg} dq_i}{\int_{Chg} dq_i} \tag{9}$$

This result is surprising, as fully reversing q_{Mn} and q_O is not a requirement using our method and its underlying assumptions. Using the same TiMS method, a spinel $LiMn_2O_4$ cathode shows irreversible q_{Mn} of ~0.1 mol e mol^{-1} after the first-discharge cutoff, (**Figure S2a, d**) which agrees with other studies employing X-ray spectroscopy.[44] This experimental agreement on the spinel not only validates our TiMS method again, but also suggests different irreversible-capacity origins between DRX and ordered cathode materials (**Figure 4a** vs. **Figure S2d**). In other words, discharged ordered materials have residual oxidized TM left from incomplete lithiation,[44,45] which governs their first-cycle irreversible capacities. On the other hand, disordered LMTO's irreversible capacity is dominated by parasitic

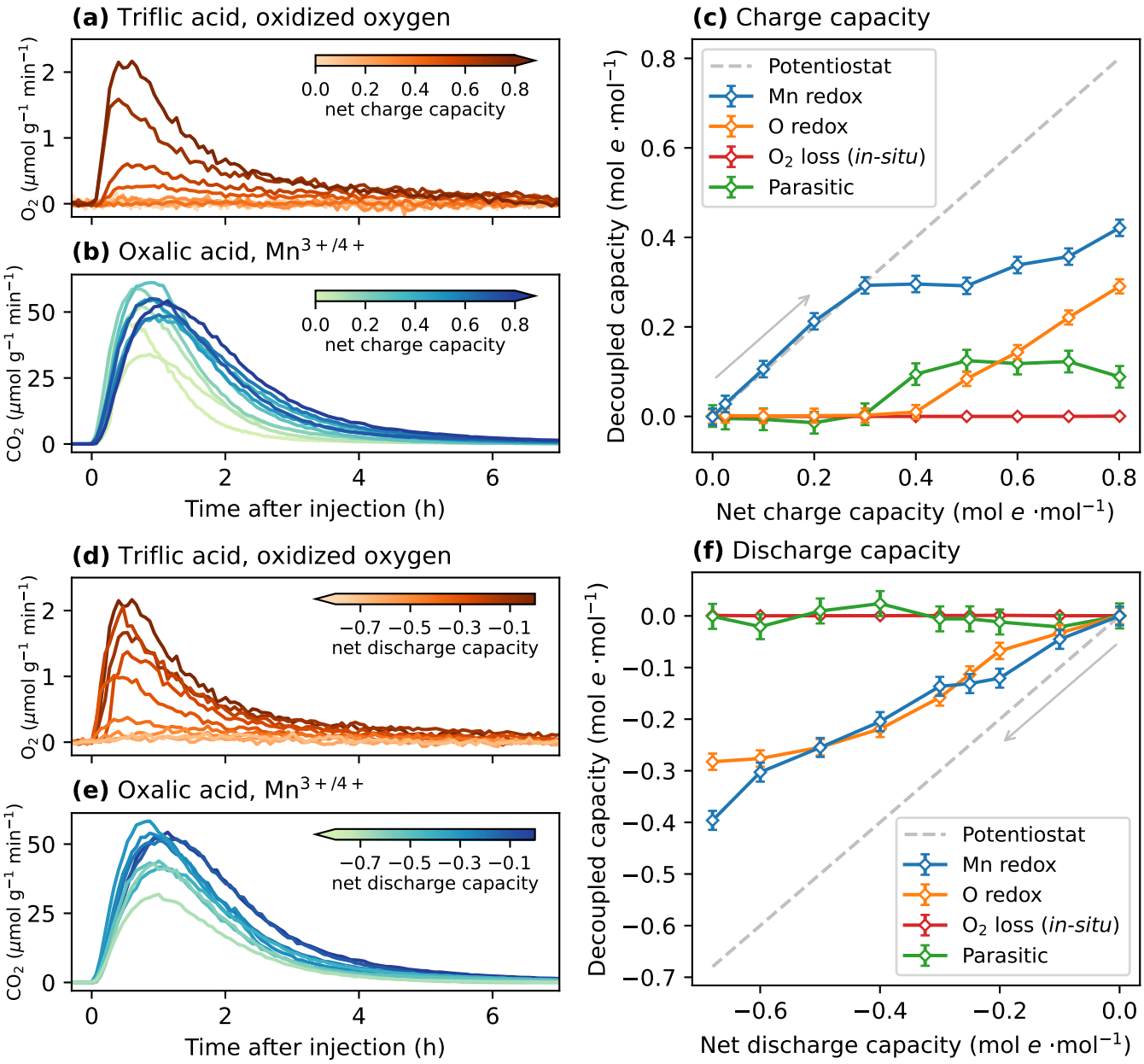

Figure 3: First-cycle redox components quantified via two-step titration. (a) O_2 evolution curves from the first (triflic acid) injection on LMTO cathodes charged to various net charge capacities (in mol e mol^{-1}). (b) CO_2 evolution curves from the second (oxalic acid) injection on charged LMTO cathodes. (c) Decoupled charge capacities plotted against net charge capacities. In-situ O_2 loss was quantified by differential electrochemical mass spectrometry (DEMS, SI Figure S8), and the back-calculated capacities follow an assumed 4 mol e per mol of O_2 loss. Interfacial parasitic capacities were derived from Equation (2): $dq_{side} = dq - dq_{Mn} - dq_O$. (d) O_2 evolution curves from the first injection on discharged LMTO cathodes. (e) CO_2 evolution curves from the second injection on discharged LMTO cathodes. (f) Decoupled discharge capacities plotted against net discharge capacities.

components ($q_{side} \approx 0.11$ mol e mol^{-1}), which implies that engineering the DRX-electrolyte interface promises to achieve a higher overall coulombic efficiency CE. To sum up, our decoupling technique reveals almost 100% reversible q_{Mn} and q_O, but their capacity-dependent profiles are different between the first charge and discharge. Given this charge-discharge discrepancy, we turn to the second cycle to see how charge compensation mechanisms evolve.

2.2.2 LMTO Second-Cycle Mn and O Redox: Reversible Faradaic Selectivity

To ensure all second-cycle LMTO cathodes underwent similar redox history, their first-cycle cutoffs were set at identical capacities, ($Chg\ q\ =\ 0.8$ and $Dchg\ q\ =\ -0.65$ mol e mol^{-1}), and each cathode was extracted within a voltage range of 4.55-1.50 V during the second cycle. **Figure 4** displays the two major redox capacities vs. net cumulative capacity, where we zero the cumulative capacity upon starting the second cycle.

During the second charge, Mn-redox capacity dominates the initial SOC range ($0 \leq q \leq 0.1$ mol e mol^{-1}, **Figure 4b**), largely reflecting the final stages of the first discharge. However, the two cycles show dissimilar redox trends on charging, which suggests that the DRX electronic band structure[14,46] changes from the beginning to the end of the full first cycle. In particular, the second-charge q_{Mn} and q_O grow together starting at roughly 50 mAh g^{-1}, while simultaneous Mn and O redox during the first charge does not commence until roughly 175 mAh g^{-1}. Turning to discharge, both cycles show Mn and O capacities with CE_i close to 100%, as round-trip q_i ends near zero vertically in **Figure 4**. Horizontally, net irreversible capacity creates a gap between zero and the first-cycle endpoint q as a result of non-zero q_{side}, while second-cycle net capacity is fully compensated by q_{Mn} and q_O. In other words, the parasitic contribution q_{side} becomes negligible at any second-cycle SOC based on Equation (2), which implies a more stable DRX-electrolyte interface after the first formation cycle.

Beyond the first cycle, Mn and O redox not only exhibit good overall reversibility in q_i, but also develop reversible faradaic selectivity (S_i) across the entire second cycle:

$$S_i = \frac{dq_i}{dq} \tag{10}$$

In other words, across the horizontal q axis in **Figure 4b**, each q_i has largely overlapping discharging and charging curves, indicating reversible S_i. This suggests that the redox combination of Mn and O capacities is only a function of the net capacity q and not a function of whether the material is being

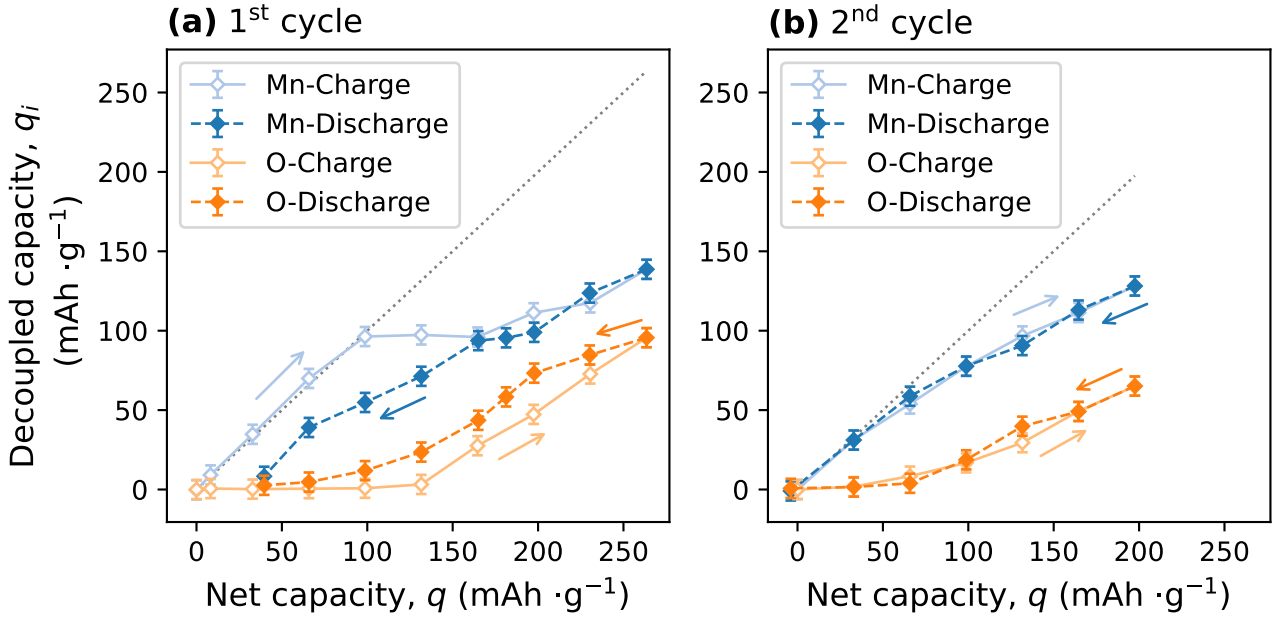

Figure 4: A comparison of Mn and O redox capacities and their faradaic selectivity for LMTO cathodes over the first two cycles. (a) First-cycle decoupled Mn-redox and O-redox capacities q_i plotted against net capacities q. As round-trip q_i ends near zero vertically, Mn and O capacities display decoupled coulombic efficiencies close to 100%, evaluated via Equation (9). (b) Second-cycle redox capacities. Mn and O redox not only exhibit high round-trip cycle reversibility during both cycles, but also develop reversible faradaic selectivity (S_i in Equation (10)) across the second cycle.

charged or discharged. Consequently, the electric-charge distribution between solid-phase $Mn^{3+/4+}$ and oxidized oxygen is identical at a given SOC regardless of whether that SOC was achieved during discharge or charge. The resolved redox trends imply that the DRX band structure remains largely unchanged after the full second cycle, as S_i becomes reversible.

To summarize, redox-reaction reversibility is twofold in our DRX material: reversible Mn and O capacities, each with close to 100% coulombic efficiency in the first two cycles; at any second-cycle SOC, faradaic selectivity is reversible, with charge-discharge path independence. Most importantly, these reversible properties are decoupled for Mn and O redox, which allows deconvolution of voltage hysteresis for each redox process.

2.3 Deconvoluted Voltage Hysteresis

To this point, we have decoupled LMTO's electrochemical properties mostly in the electric-charge dimension dq, which has not fully uncovered material hysteresis during energy storage and delivery. To access the energy scale of Mn and O redox, we must incorporate another measurable quantity — voltage V. With voltages recorded under either quasi-equilibrium or constant current, our deconvoluted voltage hysteresis further distinguishes between thermodynamic and kinetic contributions to the energy efficiency.

2.3.1 Constant-Current Energy Efficiencies are Comparable for Mn and O Redox

Operating voltage hysteresis is visualized by plotting operating voltage V_{run} vs. q_i (**Figure 5a, b**), where applied current is constant at 0.1 mol e mol^{-1} h^{-1} (defined as C/10; **Figure S10**) and voltages were recorded at each cutoff before cathode extraction for TiMS measurements. In the first charge, TiMS-decoupled Mn redox reveals two charging plateaus, with average voltages $\langle V_{run} \rangle$ = 3.50 V and 4.49 V. Upon discharge, no clear Mn-redox voltage plateau is observed, with large incremental voltage decreases at the beginning and end of the discharge. In particular, the voltage decrease at the end of discharge leads to a large charge-discharge voltage gap, exceeding 1.6 V near 0 mAh g^{-1}. This large Mn-redox voltage hysteresis reduces its round-trip energy efficiency to η_{Mn} = 74.8% — calculated from Equation (3), the trapezoidal rule, and decoupled redox capacities. In contrast, first-cycle O redox shows $\langle V_{run} \rangle$ = 4.41 V of a single charging plateau, (**Figure 5a**) whose V_{run} range is analogous to that of the upper-plateau Mn redox. Unlike the Mn-redox discharge curve, O redox shows a narrow discharging voltage with $\langle V_{run} \rangle$ = 3.37 V. As a result, O-redox charge-discharge voltage gaps are more uniform with 0.78-1.29 V mismatch, and they are larger than the upper-plateau Mn redox (voltage gaps ranging from 0.76 to 0.88 V). However, evaluation of O redox during the full charge-discharge cycle leads to an energy efficiency similar to Mn redox, (η_O = 74.3%), which surprisingly indicates that Mn redox and O redox have comparable impacts on the operating voltage hysteresis. That is, our DRX voltage hysteresis arises not just from O redox as is commonly thought for Li-excess cathode materials,[12,16] but also from lower-plateau Mn redox. It is worth noting that Mn redox exhibits similar hysteresis in a shallow-SOC cycle where no O redox is observed (η_{Mn} = 71.6% for the blue trace in **Figure 2a**). Therefore, lower-plateau voltage hysteresis is probably not linked to upper-plateau O redox across the first full cycle. When summing all redox contributions, net round-trip energy efficiency η is 67.1%, less than either the O or Mn redox due to the non-zero q_{side} contribution in the first cycle.

Turning to the second cycle, both redox voltage profiles become more sloped. Unlike the first charge, Mn-redox plateaus become less separable with the two average voltages shifted down: the lower-plateau $\langle V_{run} \rangle$ = 3.28 V; higher-plateau $\langle V_{run} \rangle$ = 4.40 V, where the ranges are discerned based on the first-cycle plateaus to allow comparison of each cycle (**Figure 5b**). Furthermore, the Mn-redox voltage profile displays small charge-discharge gaps in both the lower plateau range (0.53-0.93 V mismatch) and higher plateau range (0.72-0.74 V mismatch). On the other hand, second-charge O redox onsets earlier (at 3.26 V) than the first-charge (at 4.25 V), (**Figure 5a, b**) which leads to a wide V_{run} range and down-shifted voltage $\langle V_{run} \rangle$ = 4.10 V on charging. Analogously, charge-discharge gaps decrease to 0.26-0.92 V for

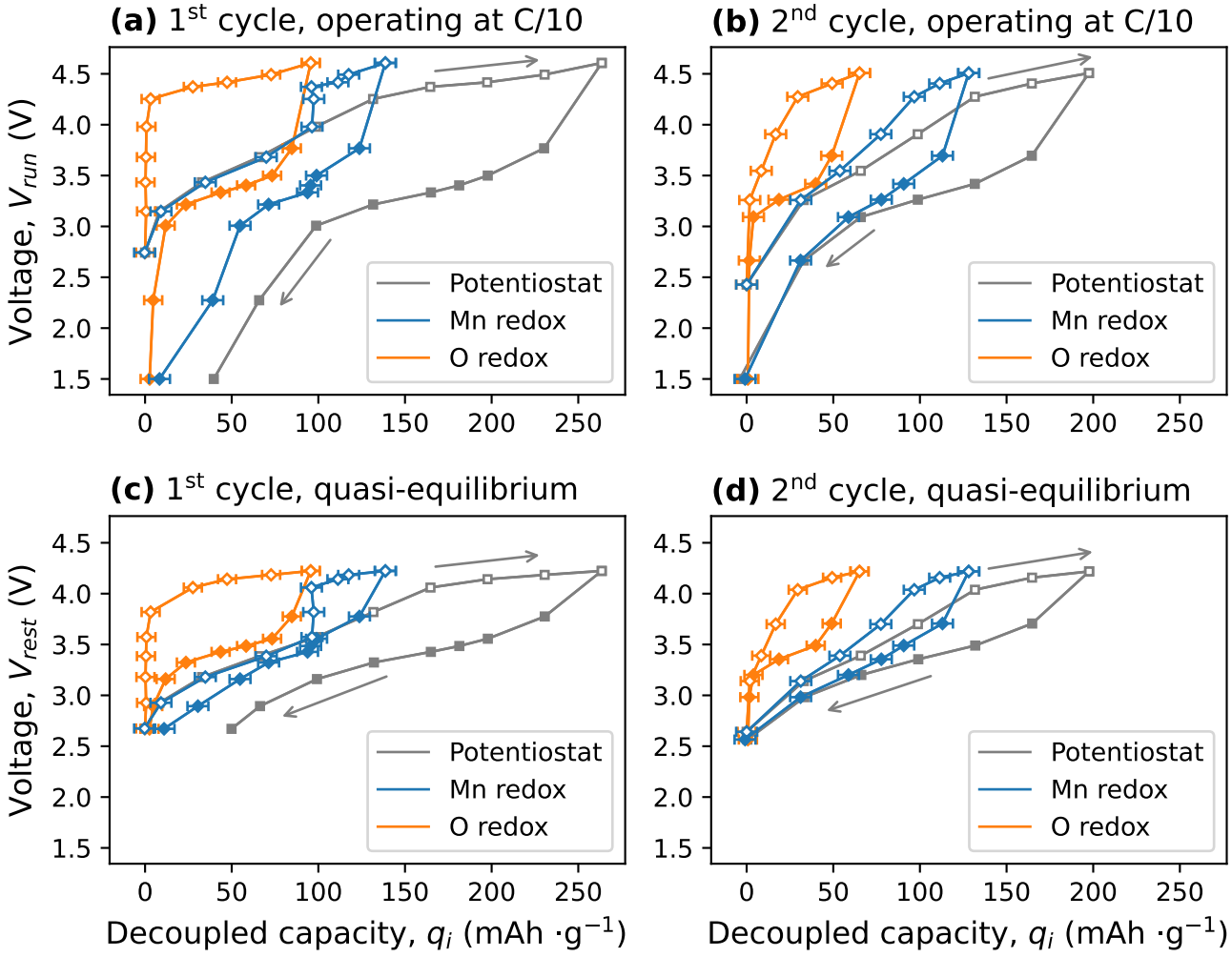

Figure 5: Decoupled redox voltage hysteresis for LMTO cathodes. (a) First-cycle operating voltage hysteresis, visualized by plotting operating voltages V_{run} against decoupled capacities q_i. C/10 rate ≡ 0.1 mol e mol^{-1} h^{-1}. Operating voltages V_{run} were measured at cut-off points within constant-current cycles (SI Figure S10). (b) Second-cycle operating voltage hysteresis. (c) First-cycle quasi-static voltage hysteresis, visualized by plotting quasi-static voltages V_{rest} against decoupled capacities q_i. Quasi-static voltages V_{rest} were measured at relaxation endpoints of a galvanostatic intermittent titration technique (GITT with 8 h relaxation between C/10 pulses, SI Figure S11). (d) Second-cycle quasi-static voltage hysteresis. All voltages are reported vs. the operating Li counter electrode, which at the low current rates used here is approximately 0 V vs. Li/Li$^+$.

second-cycle O redox. Because both redox profiles show reduced voltage gaps, their second-cycle energy efficiencies increase to η_{Mn} = 83.1% and η_O = 84.1%. Comparable efficiencies again imply that LMTO voltage hysteresis should not be ascribed to just one charge compensation mechanism, even during the first formation cycle. However, the cause for the comparable redox efficiencies η_i on each cycle remains unclear, as operating voltage hysteresis can arise from both thermodynamic and kinetic considerations. Therefore, to unfold the origin of voltage hysteresis, we need further quantitative decoupling between quasi-static (quasi-equilibrium) voltages and overvoltages.

2.3.2 Quasi-Static Energy Efficiencies and Overvoltages

To isolate kinetic overvoltages from operating voltage hysteresis, we applied the galvanostatic intermittent titration technique with 8 h relaxation between C/10 pulses, (GITT with t_{rest} = 8 h, C/10 rate ≡ 0.1 mol e mol^{-1} h^{-1}) as shown in **Figure S11**. Relaxation endpoints were recorded as

quasi-static voltages V_{rest}, which form the quasi-static voltage profiles in **Figure 5c, d**. As expected, V_{rest} curves show smaller charge-discharge hysteresis than V_{run}, which leads to net quasi-static energy efficiencies η_0 greater than operating efficiencies η, such as those during the first-cycle: $\eta_0 = 74.2\%$ vs. $\eta = 67.1\%$. Analogously, deconvoluted redox efficiencies are higher during quasi-static conditions, as can be seen by the comparison provided in **Table 1**. Even though Mn redox and O redox have similar operating energy efficiencies $\eta_{Mn} \approx \eta_O$, their intrinsic efficiencies show discernible difference, with $\eta_{0,Mn} > \eta_{0,O}$ for both cycles. Comparison among $\eta_{0,i}$ and η_i suggests that the two redox mechanisms have unequal overvoltages. In particular, Mn-redox V_{rest} charge-discharge curves almost overlap during the first-cycle lower plateau, where constant-current Mn-redox V_{run} hysteresis is much greater, particularly at low capacities (**Figure 5a, c**). In contrast, O redox does not exhibit as substantial of a difference from V_{rest} to V_{run}, with first-cycle average voltage gaps increasing from 0.62 V to 1.04 V. Because O-redox V_{rest} and V_{run} curves are similar in shape, O redox displays a more uniform overvoltage distribution than Mn redox. Therefore, the respective redox overvoltages impact the operating energy efficiency differently. To clarify operating hysteresis tied to each redox mechanism, we must quantify not only their overvoltage magnitudes, but also their overvoltage distribution.

Overvoltage distribution can be clearly visualized by plotting incremental capacities $|dq_i|dV^{-1}$ against V, where voltages are GITT-measured V_{run} or V_{rest} (detailed in **Figure 6**). Before analyzing V_{run} data, here we first focus on the quasi-static V_{rest} distribution, as it establishes equilibrium potential distributions that can then be used to evaluate overvoltages during constant-current measurements. First-charge Mn redox displays a bimodal V_{rest} distribution, while O redox has an unimodal V_{rest} distribution (**Figure 6a, c**). First-discharge V_{rest} spreads across larger voltage windows than charge for both redox mechanisms. Turning to the second cycle, the Mn and O redox $|dq_i|{dV_{rest}}^{-1}$ peaks become flattened compared to the first cycle, which implies that both Mn and O orbital-energy levels broaden in the DRX electronic band structure.[46] This widened distribution results in the bimodal Mn-redox peaks overlapping, but the O redox still has distinguishable and unimodal peaks. From V_{rest} distributions in both cycles, (**Figure 6a-d**) our redox decoupling implies that charging above $V_{rest} \approx 4.0$ V involves up-shifting depopulated orbitals to a higher energy level,[46] which results in a lower discharge $V_{rest} \approx 3.5$ V involving populating higher-energy orbitals in the DRX band structure that underlies the material's quasi-static behavior.

With quasi-static $|dq_i|{dV_{rest}}^{-1}$ providing a snapshot of LMTO's equilibrated voltage distribution, the overlaid $|dq_i|{dV_{run}}^{-1}$ shows how the voltage distribution deforms and shifts upon passing current. With C/10 current applied, both redox distributions shift nonuniformly along charge and discharge, which results in asymmetric overvoltages. However, redox overvoltage magnitudes are challenging to quantify, as they not only vary across different capacity ranges, but also differ between Mn redox and O redox. To evaluate asymmetric redox overvoltages, we define the mean overvoltage $\langle V_{over} \rangle_i$ at C/10 as the extra energy required for charge compensation via a given redox component i (Mn or O), averaged over a

Table 1: Deconvoluted energy efficiencies for Mn and O redox in LMTO cathodes.

Energy efficiency[a)]	First cycle			Second cycle		
	Mn redox	O redox	overall	Mn redox	O redox	overall
$\eta_{0,i}$	87.3%	82.6%	74.2%	93.0%	89.8%	91.9%
η_i	74.8%	74.3%	67.1%	83.1%	84.1%	83.6%

[a)] η_0 denotes quasi-equilibrium; η values were measured at C/10.

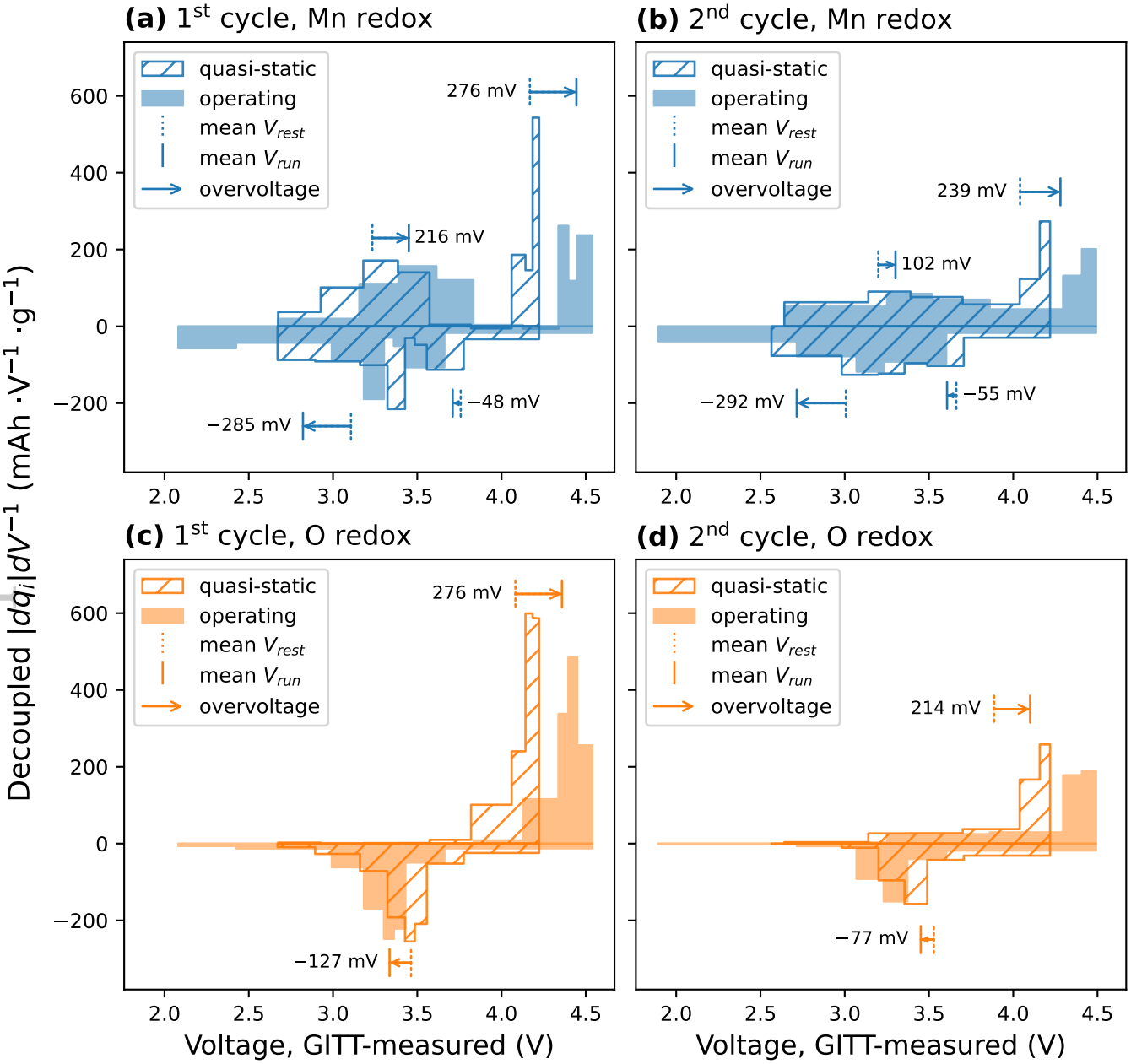

Figure 6: Deconvoluted voltage distributions and overvoltages for LMTO cathodes. (a) First-cycle Mn-redox incremental-capacity plot. Both quasi-static and operating voltages were GITT-measured (see SI Figure S11 for details of this measurement). Mean V_{rest}, mean V_{run}, and overvoltages were derived from Equation (11). (b) Second-cycle Mn-redox incremental-capacity plot. (c) First-cycle O-redox incremental-capacity plot. (d) Second-cycle O-redox incremental-capacity plot. Mean voltages for the various redox processes (O redox and low and high voltage Mn redox) are presented as vertical lines.

given redox capacity range Q:

$$\langle V_{over}\rangle_i \equiv \frac{\int_Q V_{run}dq_i - \int_Q V_{rest}dq_i}{\int_Q dq_i} = \langle V_{run}\rangle_i - \langle V_{rest}\rangle_i \tag{11}$$

A natural outcome is that the mean redox overvoltage equals the mean difference between the C/10 operating and quasi-static redox voltages, each of which are represented by vertical bars in **Figure 6**. Mn-redox overvoltages are evaluated separately in each plateau q_{Mn} range (two charge-discharge $\langle V_{over}\rangle_{Mn}$ pairs). The lower-V Mn redox has a larger discharging overvoltage than charging in both

cycles, while this comparison is flipped for the higher-V Mn redox. Intriguingly, the high-V Mn charging overvoltages are similar to the O redox overvoltages, which occur at roughly the same voltage. Because charging q_O is greater than q_{Mn} in the higher-V range, charging $\langle V_{over}\rangle_O$ is larger than $\langle V_{over}\rangle_{Mn}$ averaged across the entire charge, e.g., $\langle V_{over}\rangle_O = 276$ mV and $\langle V_{over}\rangle_{Mn} = 234$ mV throughout the first charge (including the low voltage range). On the contrary, discharging $\langle V_{over}\rangle_O$ is smaller than $\langle V_{over}\rangle_{Mn}$ across the whole discharge range, e.g., $\langle V_{over}\rangle_O = -127$ mV and $\langle V_{over}\rangle_{Mn} = -201$ mV over the entire first discharge. Furthermore, from the first to the second cycle, most of overvoltages improve, but only discharging $\langle V_{over}\rangle_{Mn}$ remains similar, which exacerbates the Mn redox kinetic limitation compared to that of O redox. Larger Mn-redox overvoltages imply that O redox does not necessarily limit DRX-like materials' kinetic performance, which answers why ultrahigh rate capability can be achieved by partial-spinel-order materials exhibiting mixed Mn and O redox.[47] To summarize, our overvoltage decoupling indicates that LMTO has variable kinetic constraints: in the mixed redox contribution range, excess charging energy is dominated by O redox; across the entire capacity range, accessible discharging energy is predominantly limited by Mn redox. Even though Mn redox has a higher quasi-static energy efficiency than O redox, LMTO operating energy efficiency is largely reduced by Mn-redox discharging overvoltage.

3 Conclusion and Broader Context

In conclusion, LMTO voltage hysteresis arises not only from intrinsic charge-discharge voltage gaps of O redox, but also kinetic limitations from Mn redox. Along the constant-current voltage hysteresis curves, our two-step titration mass spectrometry can quantify Mn and O redox capacities separately, which we found both possessed round-trip coulombic efficiencies close to 100%, even during the first (formation) cycle. Our decoupling results indicate the most effective strategy to lower net irreversible capacity for future DRX materials: suppressing interfacial side reactions during the first formation cycle. Beyond LMTO's first cycle, our technique reveals reversible faradaic selectivity between the two intermixed redox mechanisms. With redox capacities quantified incrementally, we can evaluate redox voltage hysteresis via deconvoluted energy efficiencies η_i. High quasi-static $\eta_{0,Mn}$ up to 93.0% shows the promise for developing high-efficiency DRX materials. Their future advancement should focus not only on improving quasi-static inefficiency of O redox at $\eta_{0,O} = 89.8\%$, but also on reducing discharging overvoltages that drag constant-current η_{Mn} down to 83.1%. Therefore, we anticipate that our unique analytical workflow can diagnose various DRX materials and inform valuable improvement directions, as diverse design strategies have been developed and proved effective, e.g., fluorination,[48] high-entropy TM chemistry,[49] synthetic optimization,[9] and partial spinel order.[47] With proper diagnosis and advancement in DRX materials' enormous design space, we envision that future DRX cathodes may not only feature low cost and high energy density, but also achieve high energy efficiency, which is particularly critical for EV batteries in electrifying transportation. As power grids transition from fossil fuel to sustainable energy at a slow pace, future EV cells must have high energy efficiency to further reduce equivalent CO_2 emission per mile, which thus warrants our in-depth study on the emerging DRX cathode's voltage hysteresis.

4 Experimental Section

Material synthesis: Cation-disordered rock salt $Li_{1.2}Mn_{0.4}Ti_{0.4}O_2$ (LMTO) was synthesized by a traditional solid-state method. Li_2CO_3 (Sigma, 99%), Mn_2O_3 (Alfa Aesar, 99.9%) and TiO_2 (Alfa Aesar, 99.9%) were used as precursors. All the precursors were stoichiometrically mixed in ethanol with a Retsch PM 200 planetary ball mill at a rate of 250 rpm for 12 h. 10% excess Li_2CO_3 was added to compensate for possible loss during synthesis at high temperature. The precursors were then dried in an oven at 70°C overnight and pelletized. The precursor pellets were heated to 1100°C at a rate of 9 °C min^{-1} under Ar gas flow and held for 20 min followed by cooling naturally in the furnace. To

ensure long-range phase purity, lab X-ray diffraction patterns (SI **Figure S7**) were examined using a Rigaku Miniflex 600 in the 2θ range of 15–90°. Rietveld refinement was performed using PANalytical X'pert HighScore Plus software.

Pourbaix diagram: To promote the aqueous instability of solid-phase $Mn^{3+/4+}$ in acid solution, we referred to a computed Pourbaix diagram[32] of cation-ordered $LiMn_2O_4$. The spinel $LiMn_2O_4$ pourbaix diagram was generated through open-source Python Materials Genomics (pymatgen)[50] packages. To predict solid-aqueous equilibria, the computation adopts a formalism[33] aligning experimentally tabulated aqueous-state free energies with ab initio calculated solid-state energies, which were acquired via accessing the Materials Project database.[35] As the database is actively updated, we observed slight variation in reproducing converged energy values, but their resulting Pourbaix diagram's pattern did not change. All aqueous ion concentrations were set at 10^{-6} M. Composition of metal elements is Li:Mn = 1:2, which follows unit formula of $LiMn_2O_4$ (Material ID: mp-22584). The instability map was computed from initial $LiMn_2O_4$ (s) free energy relative to equilibria-predicted states, which takes H^+ (aq), OH^- (aq), H_2O (l), and electrons into account for balancing the equilibrium reaction.[34]

Electrochemical cell assembly: To monitor in-situ gas evolution associated with interfacial parasitic reactions and O_2 loss, we measured all LMTO cathodes' voltages and net capacities in a modified Swagelok-type cell format.[51] Cathodes were prepared in an Ar-filled glove box to limit their exposure to ambient atmosphere. LMTO powder was first mortar-milled with carbon black (Super C65, TIMCAL) in 7:2 weight ratio for 30 minutes. Milled LMTO-carbon powder was then mixed with polyvinylidene fluoride (Solef 6010/1001, SOLVAY) solution in N-Methyl-2-pyrrolidone solvent (NMP, anhydrous, 99.5%, Sigma Aldrich) to form a slurry in a planetary centrifugal mixer (ARE-310, THINKY Mixer). Additional conductive carbon (Super P, TIMCAL) and NMP were added to expand the slurry to an adequate volume that enables uniform mixing in the mixer container (6 mL polypropylene container). The final solid weight composition was 62% active material, 28% carbon, and 10% binder. Slurry was cast onto a stainless-steel mesh, (120 mesh, T-316 stainless steel, TWP inc.) which allows gas to escape in the cell axial direction. After drying on a 120°C hot plate for an hour, the electrode was cut into 12 mm discs. Cathode discs were further dried overnight under static vacuum at 120°C in a heated antechamber attached to the glove box. The loading density ranged between 4.5-7.0 mg cm^{-2} for the cathode active material. Cell anodes are lithium disks in 12 mm diameter (FMC). To avoid short circuit in each Swagelok-type cell, two layers of membrane were used as the separator: a quartz microfiber disc (Whatman QM-A, cytiva) facing the cathode and a polypropylene film (Celgard 2500) facing the anode. All cell components were wet with 80 µL of 1 M $LiPF_6$ (Gotion) in ethylene carbonate/diethyl carbonate (EC/DEC, BASF, 1:1 v/v) in each cell, and they were assembled in the glove box. Constant-current experiments were tested under ambient temperature (ranged between 22-28°C), while galvanostatic intermittent titration technique (GITT, SI **Figure S11**) was carried out in a 30°C chamber (Thermotron).

Differential electrochemical mass spectrometry: We quantified the in-situ gas evolution rate from assembled cells via a custom-built system that handles gas flow from cells to a mass-spectrometry (MS) gas analyzer, which is commonly called differential electrochemical mass spectrometry (DEMS).[51] MS signals are calibrated for O_2 (research grade, Linde) and CO_2 (> 99.9%, Linde) in Ar carrier gas (ultra-high purity, Linde). To avoid interference from ambient air, each DEMS cell was leak-tested before the measurement began. A Bio-Logic VSP-series potentiostat was used to control the current passed through the DEMS cell, while voltages and net electric charge transfer were recorded every 20 seconds. Every 10 minutes, accumulated gas in each cell headspace (∼100 µL) was purged intermittently using 500 µL pulses of Ar at recorded gas pressures and room temperatures. In-situ evolved gas was sent to a holding chamber, where a variable leak valve controls sampled gas flow into a ultrahigh-vacuum chamber for MS analysis.

Titration mass spectrometry: To quantify characteristic gas products from analyte-titrant reactions, a custom-made (Adams & Chittenden, Berkeley, CA) three-neck glass vessel was used, which can be sealed

and attached to a similar gas-handling/MS system as our DEMS setup described above; we call this setup and the following procedure titration mass spectrometry (TiMS).[30] Each glass vessel has two necks, a gas inlet and outlet, connected to the gas-handling system via a combination of Ace-Thred adapters (Ace Glass Inc.), perfluoroalkoxy tubes, and Valco column end fittings (VICI AG.). The third glass neck was septum-sealed, (#7 Ace-Thred, 5037-30) which serves as a titrant injection port. Before each titration experiment, cycled cathodes were extracted from DEMS cells in the Ar-filled glove box, rinsed with 350 µL dimethyl carbonate (Gotion) three times, and dried at room temperature under vacuum for >1 h to remove residual electrolyte. Each dried cathode was sealed in a titration glass vessel in the glove box to limit their exposure to the ambient. After attaching the vessel to the TiMS system, we leak-tested and purged the vessel with Ar carrier gas to avoid interference from ambient air. All titrants were Ar-sparged for >2 h to remove residual air dissolved in the aqueous solution. A gas-tight syringe (VICI, Series C syringe with Pressure-Lok side port needle) was used to inject titrant solution, as this syringe design can avoid introducing any air into the vessel upon injection. Meanwhile, we continuously monitored vessel gas composition via MS gas analyzer to ensure that no air (MS signals: m/z = 14, 28, 32) was introduced during the injection. To destabilize solid-phase oxidized oxygen, we injected 1.5 mL of strong acid titrant, 1 M triflic acid (HSO_3CF_3 (aq)), which was selected due to its extremely negative pKa and its stable anion chemistry. After O_2 evolution attenuated, we injected 4.5 mL of 0.75 M $H_2C_2O_4$ + 0.05 M HSO_3CF_3 (aq) to chemically reduce solid-phase $Mn^{3+/4+}$, which induces oxalate-CO_2 evolution. To achieve high oxalate-CO_2 evolution rates with a stable reaction yield, oxalate titrations on LMTO cathodes were subjected to continuous illumination of a 505 nm light-emitting diode (LED) collimator (250 mW, Mightex Systems), as detailed in SI Note S2 and Note S3. Except for the LED collimator, ambient light and all other photon sources were blocked from reaching the titration glass vessels. Gas accumulated in the vessel headspace (∼5 mL) was purged by 2 mL of pulsed Ar every 2 minutes (one-channel operation) or 4 minutes (two-channel operation), noting that our TiMS setup has two separate channels with identical gas handling units to allow two cathodes to be titrated at the same time. A longer time interval between Ar pulses leads to a wider residence-time distribution of gas in the vessel headspace, but it does not change the net amount of gas collected (the area below each curve), which explains the slight differences in curve shapes in **Figure 3b**. All swept-out gas samples were subsequently quantified by the MS gas analyzer.

Supporting Information

Supporting Information is available from the Wiley Online Library or from the author.

Acknowledgements

This research was supported by the Assistant Secretary for Energy Efficiency and Renewable Energy, Office of Vehicle Technologies of the U.S. Department of Energy under Contract No. DE-AC02-05CH11231 through the Disordered Rocksalt Program (Program Managers: Peter Faguy and Brian Cunningham). T.-Y.H. gratefully acknowledges support collectively from both the Ministry of Education in Taiwan and UC Berkeley College of Chemistry through Taiwan Fellowship Program. The authors thank Laurel Wong and Tom Adams for making the titration glass vessels, and thank Douglas Scudder and Clintton Jessel for making custom fittings used in the TiMS setup. The authors thank Donghun Lee for inspiring discussions regarding cathode-material energy efficiencies in the context of industrial EV cell development. T.-Y.H. thanks Stefan Oswald, Kit McColl, Joshua J. Zak, Bin Ouyang, Fredrick Omenya, Clare P. Grey, and William Chueh for insightful discussions during the 2022 Batteries Gordon Research Conference.

References

[1] W. Li, E. M. Erickson, A. Manthiram, *Nat. Energy* **2020**, *5*, 26.

[2] W. Heijlen, G. Franceschi, C. Duhayon, K. Van Nijen, *Resour. Policy* **2021**, *73*, 102202.

[3] X. Fu, D. N. Beatty, G. G. Gaustad, G. Ceder, R. Roth, R. E. Kirchain, M. Bustamante, C. Babbitt, E. A. Olivetti, *Environ. Sci. Technol.* **2020**, *54*, 2985.

[4] Z. Yang, H. Huang, F. Lin, *Adv. Energy Mater.* **2022**, 2200383.

[5] J. Lee, A. Urban, X. Li, D. Su, G. Hautier, G. Ceder, *Science* **2014**, *343*, 519.

[6] N. Yabuuchi, M. Takeuchi, M. Nakayama, H. Shiiba, M. Ogawa, K. Nakayama, T. Ohta, D. Endo, T. Ozaki, T. Inamasu, K. Sato, S. Komaba, *Proc. Natl. Acad. Sci. U.S.A.* **2015**, *112*, 7650.

[7] R. Chen, S. Ren, M. Knapp, D. Wang, R. Witter, M. Fichtner, H. Hahn, *Adv. Energy Mater.* **2015**, *5*, 1.

[8] H. Ji, A. Urban, D. A. Kitchaev, D. H. Kwon, N. Artrith, C. Ophus, W. Huang, Z. Cai, T. Shi, J. C. Kim, H. Kim, G. Ceder, *Nat. Commun.* **2019**, *10*.

[9] Z. Cai, Y.-Q. Zhang, Z. Lun, B. Ouyang, L. C. Gallington, Y. Sun, H.-M. Hau, Y. Chen, M. C. Scott, G. Ceder, *Adv. Energy Mater.* **2022**, 2103923.

[10] R. J. Clément, Z. Lun, G. Ceder, *Energy Environ. Sci.* **2020**, *13*, 345.

[11] A. Abdellahi, A. Urban, S. Dacek, G. Ceder, *Chem. Mater.* **2016**, *28*, 5373.

[12] K. McColl, R. A. House, G. J. Rees, A. G. Squires, S. W. Coles, P. G. Bruce, B. J. Morgan, M. S. Islam, *Nat. Commun.* **2022**, *13*, 5275.

[13] R. Sharpe, R. A. House, M. J. Clarke, D. Förstermann, J.-J. Marie, G. Cibin, K.-J. Zhou, H. Y. Playford, P. G. Bruce, M. S. Islam, *J. Am. Chem. Soc.* **2020**, *142*, 21799.

[14] D. H. Seo, J. Lee, A. Urban, R. Malik, S. Kang, G. Ceder, *Nat. Chem.* **2016**, *8*, 692.

[15] N. Yabuuchi, M. Nakayama, M. Takeuchi, S. Komaba, Y. Hashimoto, T. Mukai, H. Shiiba, K. Sato, Y. Kobayashi, A. Nakao, M. Yonemura, K. Yamanaka, K. Mitsuhara, T. Ohta, *Nat. Commun.* **2016**, *7*, 1.

[16] R. A. House, G. J. Rees, M. A. Pérez-Osorio, J. J. Marie, E. Boivin, A. W. Robertson, A. Nag, M. Garcia-Fernandez, K. J. Zhou, P. G. Bruce, *Nat. Energy* **2020**, *5*, 777.

[17] I. I. Abate, C. D. Pemmaraju, S. Y. Kim, K. H. Hsu, S. Sainio, B. Moritz, J. Vinson, M. F. Toney, W. Yang, W. E. Gent, T. P. Devereaux, L. F. Nazar, W. C. Chueh, *Energy Environ. Sci.* **2021**, *14*, 4858.

[18] R. A. House, U. Maitra, M. A. Pérez-Osorio, J. G. Lozano, L. Jin, J. W. Somerville, L. C. Duda, A. Nag, A. Walters, K. J. Zhou, M. R. Roberts, P. G. Bruce, *Nature* **2020**, *577*, 502.

[19] Y. Yue, Y. Ha, T.-Y. Huang, N. Li, L. Li, Q. Li, J. Feng, C. Wang, B. D. McCloskey, W. Yang, W. Tong, *ACS Nano* **2021**, *15*, 13360.

[20] J. Hong, W. E. Gent, P. Xiao, K. Lim, D.-H. Seo, J. Wu, P. M. Csernica, C. J. Takacs, D. Nordlund, C.-J. Sun, K. H. Stone, D. Passarello, W. Yang, D. Prendergast, G. Ceder, M. F. Toney, W. C. Chueh, *Nat. Mater.* **2019**, *18*, 256.

[21] B. Qiu, M. Zhang, S.-Y. Lee, H. Liu, T. A. Wynn, L. Wu, Y. Zhu, W. Wen, C. M. Brown, D. Zhou, Z. Liu, Y. S. Meng, *Cell Rep. Phys. Sci.* **2020**, *1*, 100028.

[22] B. Li, M. T. Sougrati, G. Rousse, A. V. Morozov, R. Dedryvère, A. Iadecola, A. Senyshyn, L. Zhang, A. M. Abakumov, M.-L. Doublet, J.-M. Tarascon, *Nat. Chem.* **2021**, *13*, 1070.

[23] D. G. Marsh, D. L. Jacobs, H. Veening, *J. Chem. Educ.* **1973**, *50*, 626.

[24] D. A. Skoog, D. M. West, F. J. Holler, *Fundamentals of Analytical Chemistry*, Cengage, Mason, OH, USA **2021**.

[25] N. Birkner, S. Nayeri, B. Pashaei, M. M. Najafpour, W. H. Casey, A. Navrotsky, *Proc. Natl. Acad. Sci. U.S.A.* **2013**, *110*, 8801.

[26] S. Ramakrishnan, B. Park, J. Wu, W. Yang, B. D. McCloskey, *J. Am. Chem. Soc.* **2020**, *142*, 8522.

[27] M. J. Crafton, Y. Yue, T.-Y. Huang, W. Tong, B. D. McCloskey, *Adv. Energy Mater.* **2020**, *10*, 2001500.

[28] E. Billy, M. Joulié, R. Laucournet, A. Boulineau, E. De Vito, D. Meyer, *ACS Appl. Mater. Interfaces* **2018**, *10*, 16424.

[29] A. A. Frost, *J. Am. Chem. Soc.* **1951**, *73*, 2680.

[30] T.-Y. Huang, M. J. Crafton, Y. Yue, W. Tong, B. D. McCloskey, *Energy Environ. Sci.* **2021**, *14*, 1553.

[31] C. J. Ballhausen, *Introduction to Ligand Field Theory*, McGraw-Hill Book Company, New York, USA **1962**.

[32] W. T. Thompson, M. H. Kaye, C. W. Bale, A. D. Pelton, in *Uhlig's Corrosion Handbook* (Eds: R. W. Revie), John Wiley & Sons, Hoboken, NJ, USA **2011**, Ch. 8.

[33] K. A. Persson, B. Waldwick, P. Lazic, G. Ceder, *Phys. Rev. B Condens. Matter.* **2012**, *85*, 235438.

[34] A. K. Singh, L. Zhou, A. Shinde, S. K. Suram, J. H. Montoya, D. Winston, J. M. Gregoire, K. A. Persson, *Chem. Mater.* **2017**, *29*, 10159.

[35] A. M. Patel, J. K. Nørskov, K. A. Persson, J. H. Montoya, *Phys. Chem. Chem. Phys.* **2019**, *21*, 25323.

[36] S. E. Renfrew, B. D. McCloskey, *ACS Appl. Energy Mater.* **2019**, *2*, 3762.

[37] A. Trummal, L. Lipping, I. Kaljurand, I. A. Koppel, I. Leito, *J. Phys. Chem. A* **2016**, *120*, 3663.

[38] R. Jung, M. Metzger, F. Maglia, C. Stinner, H. A. Gasteiger, *J. Electrochem. Soc.* **2017**, *164*, A1361.

[39] L. A. Kaufman, B. D. McCloskey, *Chem. Mater.* **2021**, *33*, 4170.

[40] B. L. D. Rinkel, J. P. Vivek, N. Garcia-Araez, C. P. Grey, *Energy Environ. Sci.* **2022**.

[41] D.-H. Kwon, J. Lee, N. Artrith, H. Kim, L. Wu, Z. Lun, Y. Tian, Y. Zhu, G. Ceder, *Cell Rep. Phys. Sci.* **2020**, *1*, 100187.

[42] F. Geng, B. Hu, C. Li, C. Zhao, O. Lafon, J. Trébosc, J.-P. Amoureux, M. Shen, B. Hu, *J. Mater. Chem. A* **2020**, *8*, 16515.

[43] J. Reed, G. Ceder, *Chem. Rev.* **2004**, *104*, 4513.

[44] K. Dai, W. Shao, B. Zhao, W. Zhang, Y. Feng, W. Mao, G. Ai, G. Liu, J. Mao, W. Yang, *J. Energy Chem.* **2022**, *69*, 363.

[45] A. Grenier, P. J. Reeves, H. Liu, I. D. Seymour, K. Märker, K. M. Wiaderek, P. J. Chupas, C. P. Grey, K. W. Chapman, *J. Am. Chem. Soc.* **2020**, *142*, 7001.

[46] M. Okubo, A. Yamada, *ACS Appl. Mater. Interfaces* **2017**, *9*, 36463.

[47] H. Ji, J. Wu, Z. Cai, J. Liu, D.-H. Kwon, H. Kim, A. Urban, J. K. Papp, E. Foley, Y. Tian, M. Balasubramanian, H. Kim, R. J. Clément, B. D. McCloskey, W. Yang, G. Ceder, *Nat. Energy* **2020**, *5*, 213.

[48] B. Ouyang, N. Artrith, Z. Lun, Z. Jadidi, D. A. Kitchaev, H. Ji, A. Urban, G. Ceder, *Adv. Energy Mater.* **2020**, *10*, 1.

[49] Z. Lun, B. Ouyang, D.-H. Kwon, Y. Ha, E. E. Foley, T.-Y. Huang, Z. Cai, H. Kim, M. Balasubramanian, Y. Sun, J. Huang, Y. Tian, H. Kim, B. D. McCloskey, W. Yang, R. J. Clément, H. Ji, G. Ceder, *Nat. Mater.* **2021**, *20*, 214.

[50] S. P. Ong, W. D. Richards, A. Jain, G. Hautier, M. Kocher, S. Cholia, D. Gunter, V. L. Chevrier, K. A. Persson, G. Ceder, *Comput. Mater. Sci.* **2013**, *68*, 314.

[51] B. D. McCloskey, D. S. Bethune, R. M. Shelby, G. Girishkumar, A. C. Luntz, *J. Phys. Chem. Lett.* **2011**, *2*, 1161.

Table of Contents

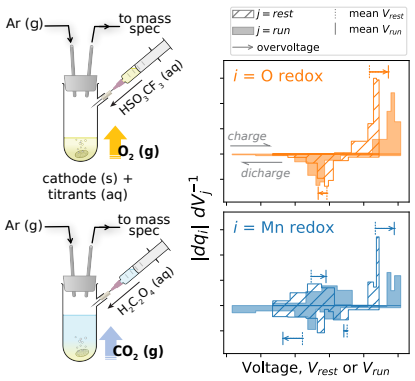

A novel two-step titration design, based on the aqueous instability of solid-phase oxidized oxygen and manganese species, is introduced to quantitatively decouple O-redox and Mn-redox voltage hysteresis in a Li-excess cation-disordered rocksalt material. A corresponding analytical workflow shows that this material's voltage hysteresis arises not only from intrinsic charge-discharge voltage mismatch of O redox, but also from asymmetric Mn-redox overvoltages.